



Nanozinc ferrites @ silica as efficient adsorbent for dye removal from wastewater: synthesis and adsorption studies

A. A. Hashem¹ · R. M. Abd El-Wahab² · M. M. A. Selim² · A. A. Badawy²

Received: 1 June 2023 / Revised: 22 December 2023 / Accepted: 3 March 2024
© The Author(s) 2024

Abstract

The precipitation process was successfully employed to prepare ZnFe_2O_4 and $\text{ZnFe}_2\text{O}_4@\text{SiO}_2$ nanoparticles. The synthesized nanoadsorbents were characterized employing transmission electron microscopy (TEM), X-ray diffraction (XRD), and Brunauer-Emmett and Teller (BET) methods. The potential adsorption capacities of the generated nanoparticles were assessed under various conditions, including pH, starting dye concentration, contact time, and temperature. The adsorption efficiency of $\text{ZnFe}_2\text{O}_4@\text{SiO}_2$ nanoparticles (95%) was higher than ZnFe_2O_4 (93%). The adsorption data were described using Langmuir, Freundlich, Temkin, and Dubinin-Kaganer-Radushkevich (DKR) isotherm models. The methylene blue (MB) removal kinetics by ZnFe_2O_4 and $\text{ZnFe}_2\text{O}_4@\text{Silica}$ nanoparticles were evaluated using linear pseudo-first-order (PFO) and pseudo-second-order (PSO) models. The removal fitted to pseudo-second-order (PSO) models as the correlation coefficient (R^2) value was (0.9994). The Boyd model may be used to validate the kinetics data, and it can be deduced that the rate-determining phase was not intra-particle diffusion, but rather the hypothesized adsorption process was endothermic and spontaneous in nature. Based on the findings, $\text{ZnFe}_2\text{O}_4@\text{silica}$ is an adsorbent material that may be useful in removing methylene blue from aqueous solutions.

Keywords Nano zinc ferrite · Silica · Adsorption · Freundlich isotherm · Boyd model

Introduction

The effective management of wastewater has attracted interest in recent decades from the agricultural, industrial, and public health sectors (Mapossa et al. 2021). Due to the numerous ways humans utilize water, highly hazardous effluents are produced, including dyes, by-products, heavy metals, and others, rendering water unfit for reusing in agriculture or human consumption (Shindhal et al. 2021). As a result, various studies have turned their attention towards water purification.

Thus, human activities release inorganic and organic wastes in large quantities resulting in polluted waters that pose a risk to human health and other living organisms (Cheng et al. 2020; Amar et al. 2021a). Dyes are one of the main contaminants that have caused widespread public concern due to their high level of visibility and toxicity to living organisms and their very negative environmental consequences if not removed from water bodies (Bangari et al. 2021; Yadav et al. 2021). Numerous process industries have made substantial use of organic dyes. The primary industrial wastewater sources have historically been the textile, paper, printing, colour photography, leather, cosmetics, and plastics industries (Hua et al. 2018).

A sizable amount of dye-contaminated water is discharged into aquatic systems by these enterprises. The majority of these colours have teratogenic, mutagenic, and carcinogenic properties (Ullah et al. 2022). Tetramethylthionine chloride, also known as methylene blue (MB), is a thiazine cationic dye that is frequently used in the textile industry to dye cotton, silk, and wood (Tsade Kara et al. 2021). When exposed to MB, one may have symptoms such as diarrhoea, vomiting, eye burns, a faster heartbeat,

Editorial responsibility: S. Mirkia.

✉ A. A. Badawy
aabadawy107@yahoo.com

¹ Faculty of Women for Arts, Science and Education, Ain Shams University, Asmaa Fahmi, Al Golf, Cairo, Egypt

² Physical Chemistry Department, Institute of Advanced Material Technology and Mineral Resources Research, National Research Centre, Cairo, Egypt



cyanosis, jaundice, excessive perspiration, quadriplegia, and confusion (Bayomie et al. 2020). Therefore, it is important for the environment to treat effluents containing methylene blue before releasing them into aquatic systems.

Toxic synthetic colours have been eliminated from contaminated water before drainage using a variety of water treatment technologies. Examples include photocatalytic degradation, electrochemical degradation, biological treatment, membrane filtration, oxidation, adsorption, ion exchange, ozonation, and more (Heidarinejad et al. 2018; Yadav et al. 2022; Yaseen and Scholz 2019; Dindorkar et al. 2022; Ibrahim et al. 2022, 2019; Badawy et al. 2020; ElHarby et al. 2019; Nady et al. 2023). Adsorption is considered to be a successful method for the removal of colourants from aqueous solution due to its unique suitability, including availability, ease of design, low working price, simplicity of process, insensitivity to harmful pollutants, with no secondary pollutant production pollutants, and high removal efficiency (Gayathri et al. 2019; Amar et al. 2018; Ghanem et al. 2020).

Due to their catalytic abilities to address environmental issues, iron oxides (Fe_2O_3) have received a lot of attention over the past ten years. The magnetic compounds known as ferrites are thought to contain mostly iron oxide. The simplicity with which these compounds may be separated by an external magnetic field following reaction, is one of their most significant advantages in the treatment of water and wastewater (Kefeni et al. 2017). The use of ferrite-based nanoparticles in sensors, biomedical, catalysis, and energy storage systems has drawn particular attention due to their exceptional adsorption powers, large surface area, optical and magnetic qualities, chemical and thermal stability, and other qualities (Liu et al. 2018; Mapossa et al. 2020; Lei et al. 2021).

Zinc ferrite (ZnFe_2O_4) is often used in water treatment operations due to its non-toxicity, strong phase resistance, visible light absorption, low cost, insolubility in water, and light corrosion resistance. The elimination of synthetic colours from wastewater using zinc ferrite has also been the subject of much study that has been shown publications (Zhao et al. 2022; Kumar et al. 2017; Mahmoodi et al. 2014; Abubaker et al. 2020).

This study sought to determine whether it was feasible and effective to use zinc ferrite/silica as a cheap adsorbent to remove methylene blue dye from solution. X-ray diffraction, transmission electron microscope, and Brunauer–Emmett–Teller (BET) analyses were employed to characterize the obtained solids. To estimate the adsorption characteristics of a chosen dye, the adsorption data were interpreted using Langmuir, Freundlich, Temkin, and Dubinin–Kaganer–Radushkevich (DKR) isotherm models and kinetic models.

Materials and methods

Materials

Ferric sulphate [$\text{Fe}_2(\text{SO}_4)_3 \cdot 7\text{H}_2\text{O}$] and zinc nitrate [$\text{Zn}(\text{NO}_3)_2 \cdot 6\text{H}_2\text{O}$] Silica (SiO_2), sodium hydroxide (NaOH), and hydrochloric acid (HCl) were purchased from Sigma-Aldrich. Methylene blue dye ($\text{C}_{16}\text{H}_{18}\text{ClN}_3\text{S} \cdot x\text{H}_2\text{O}$, $x = 2-3$) was used to study adsorption efficiency of prepared samples. All chemicals were employed as received.

Synthesis of ZnFe_2O_4 nanoparticles

Zinc ferrite (ZnFe_2O_4) was prepared by co-precipitation technique. Briefly, ferric sulphate and zinc nitrate were added to distilled water at a nominated molar ratio ($\text{Fe}/\text{Zn} = 5$). The precipitating agent used was ammonia solution (1 M) till pH 7, while the temperature was kept at 80 °C. pH measurements were taken by using pH meter (Jenway model 3505, UK). Distilled water was employed to wash the precipitate for removing of NO_3^- , SO_4^{2-} , and NH_4^+ ions. The as-prepared solid was subsequently filtered, dried at 100 °C overnight, and then calcined for four hours at 600 and 800 °C.

Synthesis of ZnFe_2O_4 @silica nanoparticles

ZnFe_2O_4 @Silica nanoparticles were obtained by treating a definite obtained powdered as mixed hydroxides with certain amount of silica (0.05 mol%), which was dissolved in small amount of distilled water sufficient to obtain a paste. The obtained paste was dehydrated at 100 °C and then heated for 4 h at 600 and 800 °C.

Characterization of synthesized nanoparticles

Crystal structure of the produced oxides was investigated using X-ray diffraction on a Bruker D 8 advance target with $\text{CuK}\alpha$ as the radiation source, at a scanning rate of 0.2 min^{-1} , 40 kV, 40 mA, and a wavelength of 1.5405 nm for line broadening profile analysis. An electron microscope (TEM, Model: JEOL-JEM-1400) was used to obtain the images. JASCO-V-730-Japan, in the range from 1000 to 200 cm^{-1} , was used to confirm the adsorption of dyes on the best adsorbent. With the help of Quantachrome Instruments (Germany), the surface area (S_{BET}) and pore size distribution of all obtained solids were calculated using the BET method and N_2 gas. Prior to analysis, the

recovered solids were degassed at 120 °C for 6 h. ANOVA was used in the statistics.

Adsorption studies

Adsorption experiments

A predetermined weight of the dye was dissolved in bi-distilled water to create a stock solution. Dilutions were used to create the appropriate concentrations for the adsorption experiments from the stock solution. Following observations using a single-beam UV–Vis spectrophotometer (JASCO V-730, Japan), a curve was utilized to determine the concentration at each experiment. For kinetic and equilibrium investigations, absorbance measurements were transformed into concentrations using this curve.

For the adsorption of reactive MB dye solution from aqueous solution, batch equilibrium approach was utilized. After shaking 50 mg of the adsorbent with 100 mL of dye solution of the determined primary concentration, the solutions were allowed to settle for three hours at a certain pH (25 ± 0.1 °C). Studies of equilibrium isotherms were conducted using different primary concentrations, ranging from 10 to 200 ppm. To investigate the adsorption process, models of the Langmuir, Freundlich, Temkin, and Dubinin–Radushkevich (D–R) isotherms were used.

Additionally, at 25 °C, 50 mg of adsorbent, contact times ranging from 0 to 3 h with stirring at 150 rpm, and at pH 7, the impact of dye concentrations varying between 10 and 200 ppm was investigated. The solutions were centrifuged at 7000 rpm for 10 min, and then they were examined using a single-beam UV–Vis spectrophotometer (JASCO V-730, Japan) at the proper MB dye wavelength (664 nm).

The pH is a significant factor that influences how well dye molecules were adsorbed. Thus, using a pH-meter (Jenway model 3505, UK), it was possible to fix the beginning dye concentrations in our investigation at 50 ppm and a pH range of 2–8 (using 0.1 M of HCl and/or NaOH). The effects of solution pH on the removal percentage (R%) were investigated. In order to determine the time to equilibrium at pH 7, the influence of time was investigated using initial concentrations of 50 ppm at 25 °C. Kinetic experiments were identical to equilibrium testing, with the exception that they take three hours to reach equilibrium. To determine the amount of MB adsorbed at any given time (q_t), the quantity of MB adsorbed at equilibrium (q_e), and the ratio of MB uptake (%R), the following equations (Hajjaligol and Masoum 2019) were used:

$$q_t = \frac{(C_0 - C_t) \times V}{m} \quad (1)$$

$$q_e = \frac{(C_0 - C_e) \times V}{m} \quad (2)$$

$$\text{Removal(\%)} = \frac{(C_0 - C_e)}{C_0} \times 100 \quad (3)$$

where C_e and C_t were the ending dye concentrations (mg/L) at time t and at equilibrium, respectively. C_0 was the beginning dye concentrations (mg/L). V was the dye solution volume in litres, and m was the adsorbent dose in grams.

Adsorption kinetic models

Pseudo-first-order (PFO) and pseudo-second-order (PSO) kinetic models are most frequently employed to fit the collected experimental data and better understand the kinetics of the adsorption process. The linear forms of PFO (Eq. 4) and PSO (Eq. 5) can be described as follows (Tran et al. 2017):

$$\ln(q_e - q_t) = \ln q_e - K_1 t \quad (4)$$

$$\frac{t}{q_t} = \frac{1}{k_2 q_e^2} + \frac{t}{q_e} \quad (5)$$

where q_e and q_t are as previously mentioned. PFO and PSO have rate constants K_1 (min^{-1}) and K_2 ($\text{g/mg}\cdot\text{min}$), respectively. From the intercept and slope of the plot of $\ln(q_e - q_t)$ vs. t , it is possible to determine the values of q_e and K_1 , respectively. Using the intercept and slope of the plot of t/q_t vs. t , respectively, the values of K_2 and q_e were computed.

Adsorption mechanism

Rate-determining step prediction is essential for the design's goal. For a solid–liquid adsorption process, the solute transfer is frequently described by either external mass transfer, intra-particle diffusion, or both. The three sequential processes shown below (Vadivelan and Kumar 2005) can be used to describe the adsorption dynamics: Moving the solute from the bulk solution through the liquid film to the adsorbent outer surface was the initial stage. Except for a little quantity of sorption on the exterior surface, the second step entailed solute diffusion inside the pore of the adsorbent. The final step involved solute sorption on the interior surfaces of the pores and capillary spaces of the adsorbent. The slowest process, which could be either film diffusion or pore diffusion, would regulate the overall rate of sorption.

a. Intra-particle diffusion equation

The intra-particle diffusion equation (Asfaram et al. 2015) was provided as:



$$q_t = K_{id}t^{0.5} + C \quad (6)$$

where C stands for the thickness of the boundary layer and K_{dif} is ($\text{mg g}^{-1} \text{min}^{-1/2}$).

a. Boyd plot

The Boyd plot accurately predicts the real slow phase in the adsorption process. The Boyd kinetic expression:

$$F = 1 - (6/\pi(22)2) \exp(-B_t) \quad (7)$$

where B_t is a mathematical function of F . F stands for the percentage of solute adsorbed at any given time t .

$$B_t = -0.4977 - \ln(1 - F) \quad (8)$$

Adsorption isotherm models

Four well-known models, Langmuir, Freundlich, Temkin, and Dubinin, were used to determine the adsorption isotherms and to describe the nature of the interaction between MB and zinc ferrite. With varied initial dye concentrations (10–200 ppm), the observed experimental adsorption data were fitted using these empirical isotherm models. The Langmuir isotherm model is employed to describe monolayer adsorption that occurs on a homogeneous surface (Vadivelan and Kumar 2005). The Langmuir equation is represented by Eq. 9 as follows in its linearized form (Langmuir 1916; Lim et al. 2017):

$$\frac{C_e}{q_e} = \frac{1}{q_m K_L} + \frac{C_e}{q_m} \quad (9)$$

where K_L is the Langmuir constant (mg/g) and q_{\max} is the maximum quantity of MB that can be adsorbed (mg/g). The slope and intercept of the linear plot of C_e against C_e/q_e could be used to get the values of q_{\max} and k_L , respectively. The separation factor (R_L), a parameter that may be computed using the following equation, can be used to determine the viability of the Langmuir adsorption isotherm.

$$R_L = \frac{1}{1 + K_L C_o} \quad (10)$$

where C_o is the initial concentration of adsorbate (mgL^{-1}) and b is the Langmuir constant (mg/g), which measures the affinity of binding sites. The R_L value, which might be favourable ($0 < R_L < 1$), unfavourable ($R_L > 1$), linear ($R_L = 1$), or irreversible ($R_L = 0$), determines the isotherm type (Weber and Chakravorti 1974).

The multilayer adsorption process takes place on a heterogeneous surface, according to the Freundlich isotherm model's

premise. The linearized version of the Freundlich equation (Freundlich 1906) is:

$$\ln q_e = \ln K_F + \frac{1}{n} \ln C_e \quad (11)$$

where K_F is the Freundlich constant (mg/g) and n is the dimensionless adsorption intensity, which indicates surface heterogeneity. The n values can be used to confirm the different forms of adsorption. The slope ($1/n$) and K_F value, which were determined from the intercept ($\ln K_F$) of the linear plot, could be obtained from the linear plot of $\ln C_e$ against $\ln q_e$. Linear ($n = 1$), unfavourable ($n > 1$), favourably ($n < 1$), and irreversibly ($n = 1$) describe the adsorption process.

According to the Temkin model, adsorbent–adsorbate interactions cause all of the molecules in the layer's heat of adsorption (a function of temperature) to decrease linearly with surface coverage. The equation is presented in its linear version as (Dada et al. 2017; Temkin and Pyzhev 1940):

$$Q_e = \frac{RT}{b_T} \ln k_T + \frac{RT}{b_T} \ln C_e \quad (12)$$

k_T is the equilibrium Temkin isotherm binding constant (L/g), and b_T is the Temkin isotherm constant, corresponding to the heat of adsorption, where $B = RT/b_T$. The values of these constants were computed using the slope and intercept of the relevant Q_e versus $\ln C_e$ plot.

The adsorption mechanism with a Gaussian energy distribution onto a heterogeneous surface is typically explained using the Temkin and Dubinin-Kaganer-Radushkevich (DKR) isotherm model. The given linear equation is (Dubinin 1965)

$$\ln Q_e = \ln Q_d - A_{DKR} \epsilon \quad (13)$$

where Q_d is the hypothetical isotherm saturation capacity (mg/g) and A_{DKR} is the DKR isotherm constant (mol^2/kJ^2) related to free adsorption energy. The slope and intercept of the $\ln Q_e$ versus ϵ^2 plot were used to get the values of A_{DKR} and Q_d . The Polanyi potential, which is the parameter ϵ , is calculated as follows:

$$\epsilon = RT \ln \left[1 + \frac{1}{C_e} \right] \quad (14)$$

Adsorption thermodynamics

Gibb's free energy (ΔG°), enthalpy (ΔH°), and entropy (ΔS°), which may be calculated using the following formulae (Lim et al. 2017; Dinh et al. 2019), were used to explain the adsorption thermodynamics:

$$\Delta G^\circ = \Delta H^\circ - T \Delta S^\circ \quad (15)$$



$$\ln K_c = -\frac{\Delta H^\circ}{RT} + \frac{\Delta S^\circ}{R} \quad (16)$$

$$K_d = \frac{c_s}{c_e} \quad (17)$$

where C_s is the amount of MB present on the adsorbent surface (in mg/L), T is the absolute temperature (in K), and K_c is a constant known as the distribution coefficient, where R (the gas constant) is equal to 8.314 J/mol.K. The values of ΔH° (J/mol) and ΔS° (J/mol) were determined using the slope and intercept of the plot $\ln K_c$ against $(1/T)$, respectively.

(f) Desorption studies

Desorption and regeneration studies have been conducted to look into the potential repeatability of using zinc ferrite or zinc ferrite@silica. In general, 0.2 g/L of the MB dye concentration and 0.12 g (100 mL) of the adsorbent were mixed for 180 min. It determined what the analyte's ultimate concentration was. Following the adsorption cycle, the MB-loaded nanoparticle was eluted under the same operating conditions as stated above, using various concentrations of the desorbing agent HNO_3 . The desorbed nanoparticles were utilized as the regenerated adsorbent for the subsequent adsorption cycle after the supernatant's MB dye content was determined.

Results and discussion

X-ray diffraction measurements

Figure 1 shows the X-ray diffractogram of the synthesized adsorbents calcined at 600 and 800 °C. Figure 1a illustrates a mixture of rhombohedral Fe_2O_3 as a major phase (63.1%) and cubic ZnFe_2O_4 as a minor phase (36.9%) according to PDF 890599 and 221,012, respectively. The phase of ferric oxide gives the diffraction lines of 2θ at 24.2°, 33.2°, 35.6°, 40.8°, 49.4°, 54.1°, 57.6°, and 64°; their d (Å) values are 3.68, 2.70, 2.52, 2.20, 1.84, 1.69, 1.60, and 1.45 with corresponding planes (012), (104), (110), (113), (024), (116), (018), and (300), respectively. The zinc ferrite phase gives pattern at $2\theta = 18.2^\circ, 29.9^\circ, 35.3^\circ, 36.9^\circ, 42.8^\circ, 53.1^\circ, 56.6^\circ, \text{ and } 62.2^\circ$; their d (Å) values are 4.87, 2.98, 2.54, 2.44, 2.11, 1.72, 1.62, and 1.49, corresponding to the planes (111), (220), (311), (222), (400), (422), (511), and (440), respectively. Raising calcination temperature to 800 °C (Fig. 1b) resulted in the appearance of ZnFe_2O_4 as the major phase and Fe_2O_3 as the minor phase. With SiO_2 -treated solids and calcined at 600 °C no sharp peaks were recorded (Fig. 2a), only a broad peak at about $2\theta = 17 - 29^\circ$ with a low degree of crystallinity due to the presence of amorphous nanosilica. A similar X-ray diffractogram was previously given for amorphous silica (Maddalena et al. 2019). For the sample obtained and calcined at 800 °C (Fig. 2b), the characteristic peaks of ZnFe_2O_4 begin to appear as a major phase with low intensity and those for Fe_2O_3 with very low intensity.

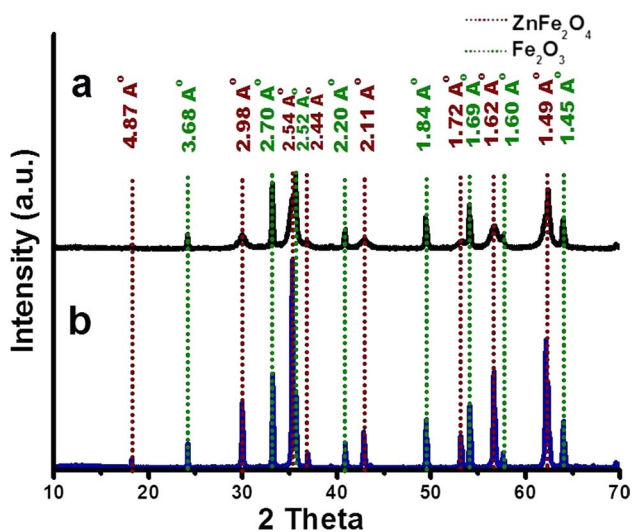


Fig. 1 X-ray diffractogram of the synthesized adsorbents **a** calcined at 600 °C and **b** at 800 °C in the absence of silica

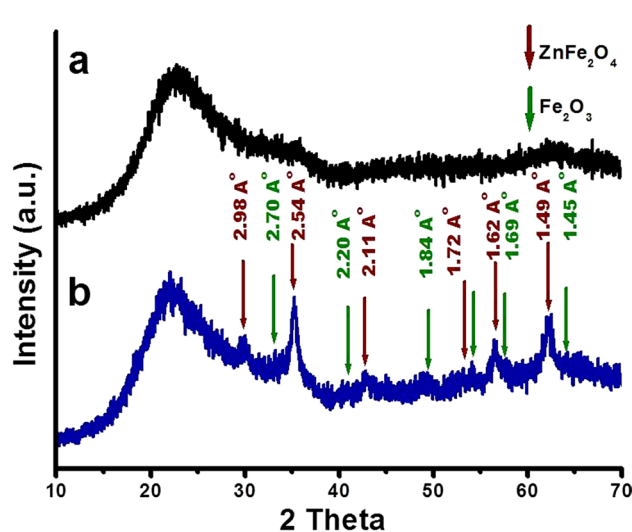
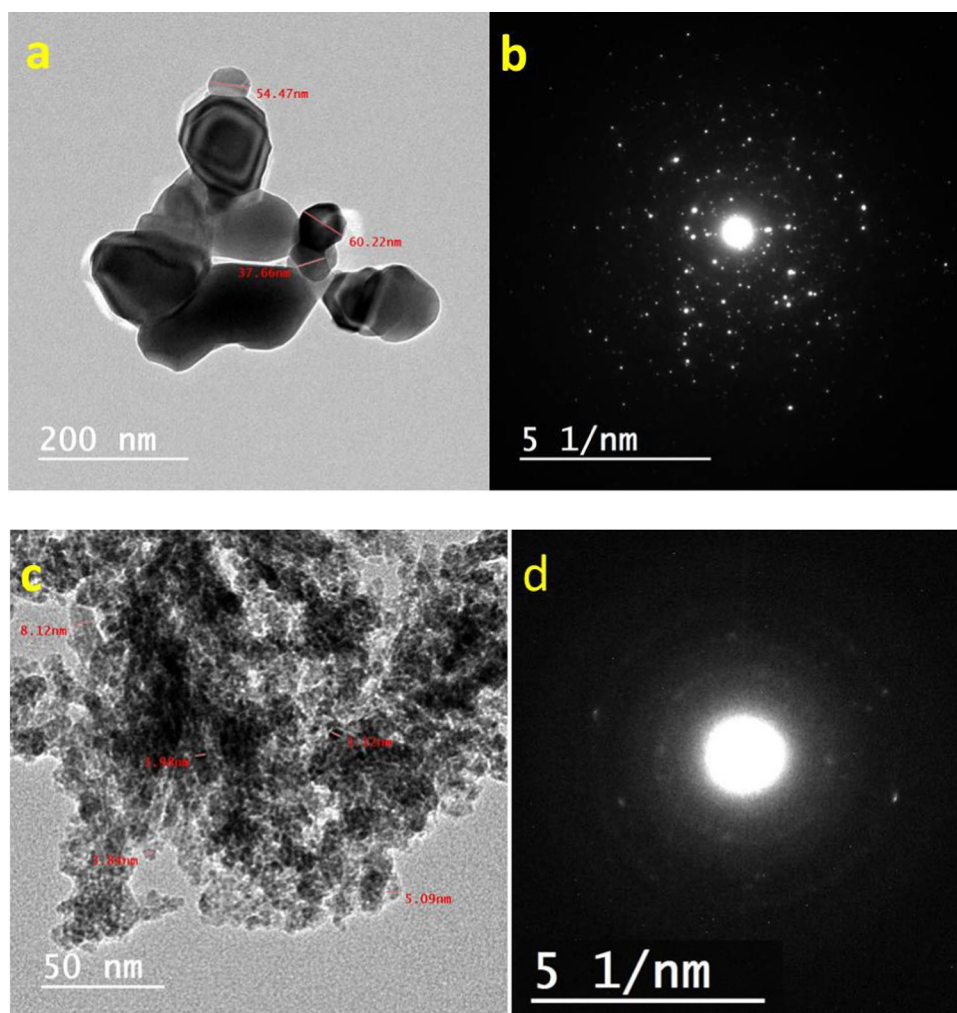


Fig. 2 X-ray diffractogram of the synthesized adsorbents **a** calcined at 600 °C and **b** at 800 °C in the presence of silica



Fig. 3 HRTEM images (a and c) and diffraction patterns (b and d) of the prepared adsorbents and SiO₂-treated via impregnation, respectively, calcined at 800 °C



TEM measurements

High-resolution transmission electron microscopy images were used for the evaluation of the surface properties of the prepared adsorbents. Figure 3a represents the prepared adsorbents calcined at 800 °C. The images confirmed the cubic and rhombohedral structures of ZnFe₂O₄ and Fe₂O₃, respectively, as previously explained by XRD analysis (c.f. Sect. "X-ray diffraction measurements"). The diffraction pattern of the prepared sample at 800 °C, Fig. 3b, confirmed the developed crystallinity of the obtained powder. Figure 3c exhibits a SiO₂-treated sample at 800 °C. Nanostructure particles with a narrow size distribution were observed. The amorphicity of the nanoparticles is confirmed in Fig. 3d. The results obtained were in good agreement with the data obtained by XRD.

Surface studies

The prepared samples' N₂ adsorption/desorption isotherms are shown in Fig. 4. The investigations of Fig. 4 and Table 1

revealed a significant effect on surface properties by increasing the temperature from 600 to 800 °C. The values of surface area for the solids prepared in absence of silica were reduced from 67.4 to 42.83 m²/g. The same trend for total pore volume is from 0.3134 to 0.0840 cc/g, and also mean pore diameter from 18.60 to 7.85 nm.

Meanwhile, in the presence of silica, raising the temperature from 600 to 800 °C improves the surface characteristics. Surface area grew from 134.03 to 168.17 m²/g, total pore volume increased from 0.5396 to 0.8431 cc/g, and mean pore diameter increased from 16.10 to 20.05 nm, respectively, keeping on the same behaviour of adsorption–desorption isotherm as observed in Fig. 4 which was characteristic to type IV. The type IV isotherm was distinguished by its hysteresis loop, which was connected to capillary condensation occurring in mesoporous, thus restricting uptake over a broad range of high P/P⁰. It was intended for the closed hysteresis loop to be H1, which denotes agglomerates or spherical particles grouped in a largely homogeneous manner. Cylindrical pore geometry denotes comparatively high pore size uniformity and simple pore connectivity. It could

Fig. 4 Nitrogen adsorption–desorption isotherms and pore size distribution according to the NLDFT method of samples calcined at 600 and 800 °C in the absence (a, b), (c, d) and presence of silica (e, f) and (g, h), respectively

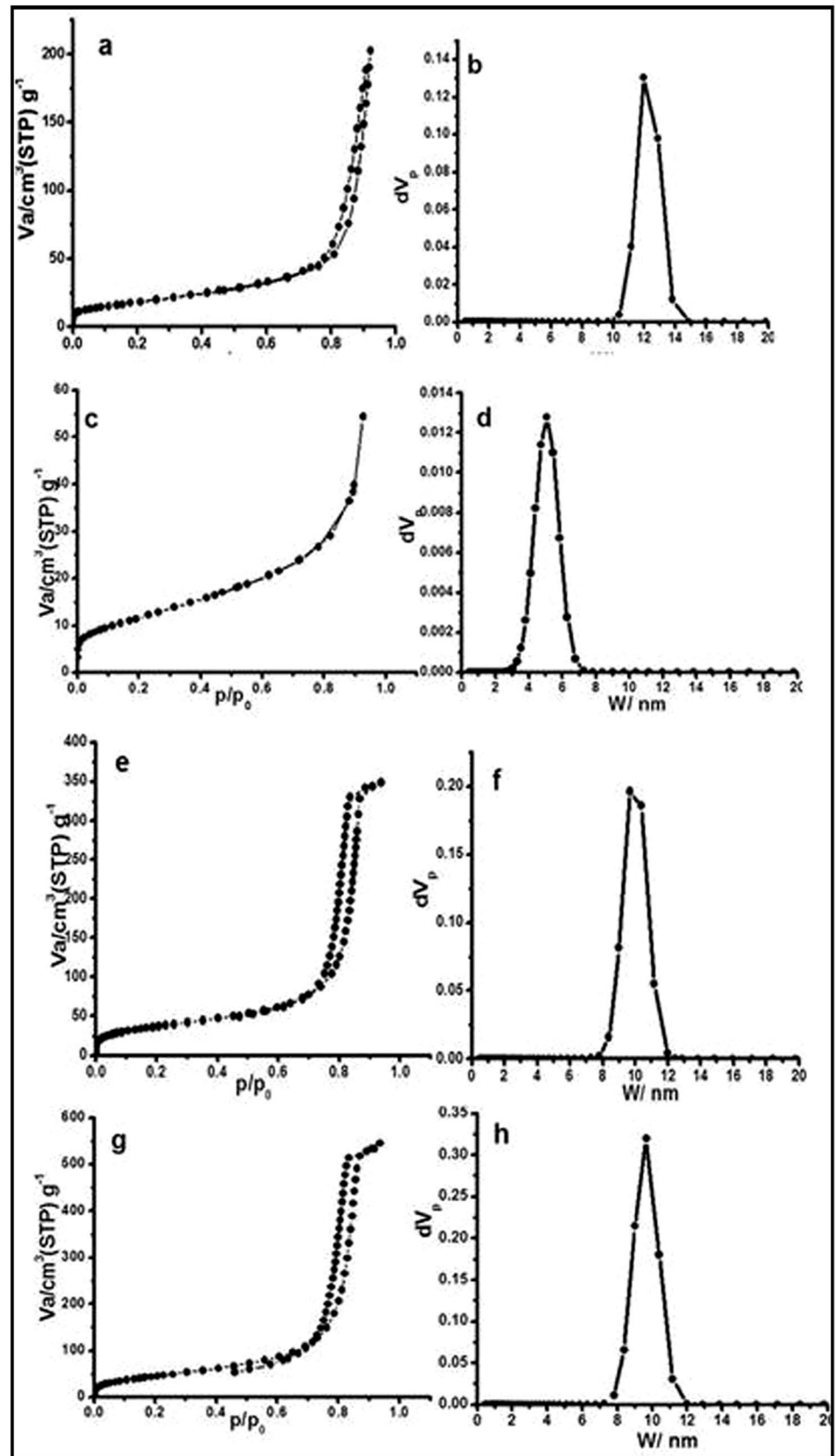


Table 1 Surface characteristics of obtained solids after calcination at various temperatures 600 and 800 °C

Adsorbent	Calcination temperature, °C	S_{BET} , m ² /g	Total pore volume (V_p), cc/g	Mean pore radius (r^-), nm
ZnFe ₂ O ₄	600	67.4	0.3134	18.60
ZnFe ₂ O ₄	800	42.83	0.0840	7.85
ZnFe ₂ O ₄ @ silica	600	134.03	0.5396	16.10
ZnFe ₂ O ₄ @ silica	800	168.17	0.8431	20.05

be noticed that the pore size distribution for all samples exhibits a narrow distribution of mesoporous pore diameters.

Effect of operational parameters on dye adsorption

Effect of solution pH

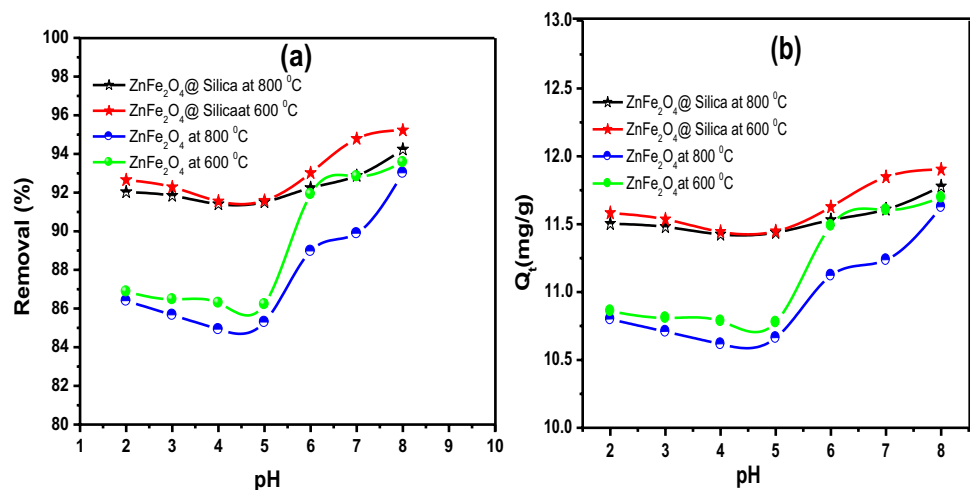
The effects of pH (from 2 to 8) were investigated at a fixed initial MB concentration of 100 mg/L, an adsorbent dosage of 0.2 g/25 mL, and duration of 60 min. To get the pH of the solution to the correct level, HCl and NaOH were utilized. The uptake efficacy of MB (%R) and amount of MB adsorbed (q_t , mg/g) as a function of solution pH are shown in Fig. 5. It can be clearly seen that the order of %R and q_t as ZnFe₂O₄@ silica activated at 600 °C > ZnFe₂O₄@ silica activated at 800 °C > ZnFe₂O₄ activated at 600 °C > ZnFe₂O₄ activated at 800 °C and raised dramatically with elevating pH and getting maximum values to 93.56 for ZnFe₂O₄ at 600 °C and 95.22 for ZnFe₂O₄@ silica that at 600 °C at pH 8. When dissolved in water, the cationic dye MB releases positively charged ions. On the other hand, a rise in the electrostatic attraction between the cationic dye (positive ions) and the negatively charged surface of ZnFe₂O₄ may be the cause of the high %R and q_t values at pH 8. As

stated (Al-Anber et al. 2011), it is anticipated that the Cl⁻ (MB-S + Cl⁻) and NaOH-containing MB dye will undergo a replacement reaction, resulting in the synthesis of NaCl and (MB-S + OH⁻). Therefore, it is possible that the elevated values of %R and q_t at pH levels over 6 are caused by the creation of NaCl, which also increases the ionic strength of the solution. ZnFe₂O₄@ silica gives higher removal efficacy than ZnFe₂O₄ nanoadsorbent calcined at 600 °C. By noting the reduction in the active phase ZnFe₂O₄'s crystallite size (cf. Sect. "X-ray diffraction measurements") and raising the S_{BET} for ZnFe₂O₄@ Silica calcined at 600 and 800 °C (cf. Table 2), this finding may be explained by the efficacy of increasing the uptake of MB.

Effect of contact time

By varying the contact duration while maintaining the other experimental parameters (pH 7, starting MB concentration of 100 mg/L, and adsorbent dose of 0.2 g/25 mL) at constant values, we looked at how contact time affected the q_t (mg/g) and % R of MB. The final outcomes are shown in Fig. 6. The findings demonstrated that when contact time extended and adsorbents were activated at 600 °C, the percentage R and values of q_t reached their maximum values than that activated at 800 °C of about 11.81 and 11.95 mg/g for ZnFe₂O₄ and ZnFe₂O₄@ silica at 130 min, respectively.

Fig. 5 Effect of starting pH on the amount of MB removed a and the capacity for adsorption b



Also, the % removal increased by increasing contact time, while the adsorbent ZnFe₂O₄ @silica that activated at 600 °C has highly removal efficiency with value 95.62% and ZnFe₂O₄ activated at 600 °C has % removal reached to 94.44%. At the beginning of adsorption, the adsorption rate remains constant and then it significantly raised with the elevating the time of adsorption. This was because, at the start of adsorption, there is an equilibrium state for MB at the surface of adsorbents and then a great amount of active adsorption sites on the surface of the adsorbents could be used, causing a fast adsorption rate. The presence of different active sites, such as Fe₂O₃ and ZnFe₂O₄ or reducing the

active sites' crystallite size, pushes the surface in order to increase the absorbance quality.

Effect of initial dye concentration

By changing the MB concentration from 10 to 200 mg/L, the impact of the initial dye concentration was investigated. A considerable change in the %R of MB was detected with raising the primary concentration from 10 to 200 mg/l, as shown in Fig. 7, which demonstrated the reliance of the %R and the q_t of MB dye on the primary concentration of MB. Figure 7 shows that ZnFe₂O₄@silica activated at 600 °C

Table 2 Thermodynamic parameters for adsorption of MB by ZnFe₂O₄ and ZnFe₂O₄ @Silica nanoparticles

Adsorbent	Calc. temp., °C	ΔH° (KJ/mol)	ΔS° (J/mol.K)	ΔG° (kJ/mol)					
				298 k	303 K	308 K	313 K	318 K	323 k
ZnFe ₂ O ₄	600	7.522	20.219	1.807	1.543	1.482	1.268	1.133	0.661
ZnFe ₂ O ₄	800	8.326	22.219	2.018	1.837	1.751	1.402	1.157	0.863
ZnFe ₂ O ₄ @ silica	600	5.097	17.446	0.070	-0.031	-0.119	-0.297	-0.433	-0.826
ZnFe ₂ O ₄ @ silica	800	9.462	30.489	0.730	0.508	0.209	-0.032	-0.185	-0.826

Fig. 6 Effect of contact duration on MB removal rate **a** and adsorption capacity **b**

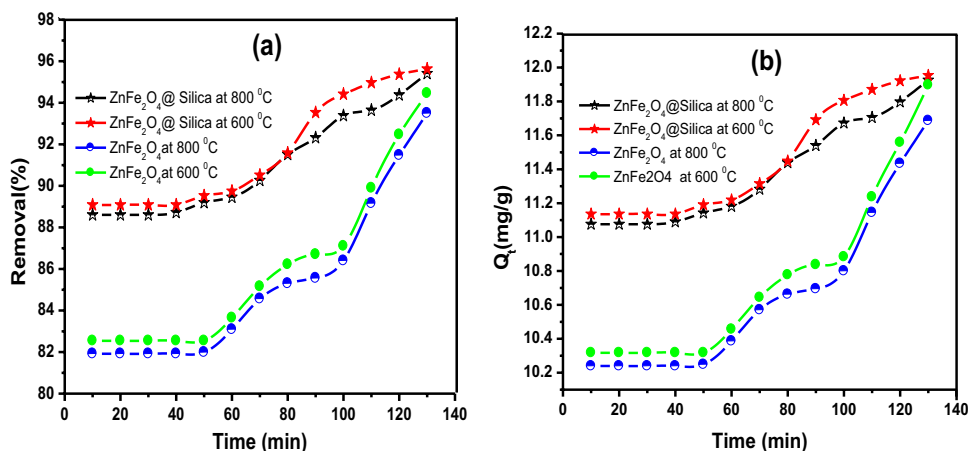
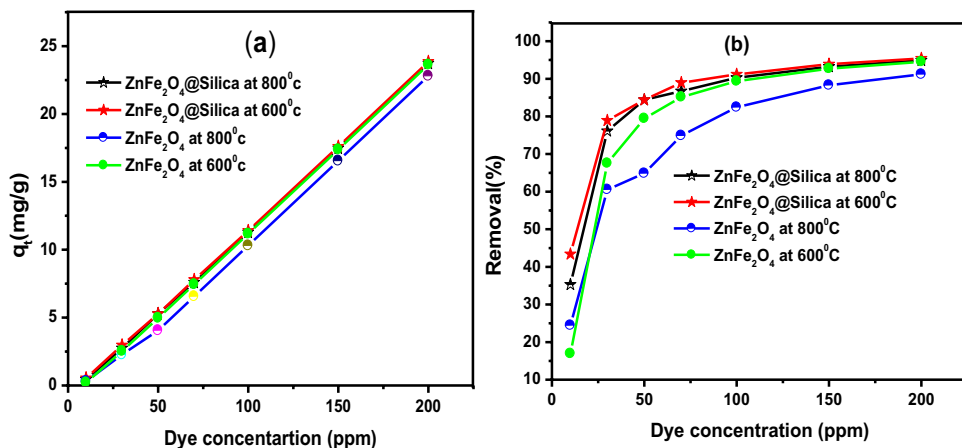


Fig. 7 Effect of initial dye concentration on the amount of MB removed and the capacity for adsorption



was more active than that activated at 800 °C, which the removal % increases from 43.39 to 95.405% for that activated at 600 °C, while in case of that activated at 800 °C the removal % increases from 35.30 to 94.909%. With respect to ZnFe_2O_4 only also the one activated at 600 °C more active than that activated at 800 °C in which removal % reaches to 94.52 and 91.21%, respectively. Finally, we observed that the ZnFe_2O_4 @silica is more active than ZnFe_2O_4 . Therefore, 100 mg/l was determined to be the ideal MB concentration. The q_t value for ZnFe_2O_4 activated at 600 and 800 °C, respectively, is different from the %R of MB and increased considerably from 0.2116–23.631, 0.308–22.804 mg/L. The % R of MB and the q_t value raised from 0.542–23.851 and 0.441–23.727 mg/g for that ZnFe_2O_4 @silica activated at 600 and 800 °C as primary concentration was raised from 10 to 200 mg/L. The fact that the dye's high primary concentration will afford the required motivation to transport the MB molecules from the bulk present in liquid phase to the surface of adsorbent present in solid states serves as an example of this. Moreover, the improvement in the adsorbent–dye interaction brought on by raising the initial dye concentration may also contribute to the rise in the value of q_t (Huang et al. 2018).

Effect of temperature of the solution

Under the aforementioned optimized operational circumstances, the impact of temperature on the remove of MB onto nanoparticles was inspected at a range of temperatures (25–50 °C). In Fig. 8, elevating the temperature led to an increase in the q_t value as well as the %R of MB. This may be because raising the temperature will raise the dye molecules' kinetic energy, increasing their interaction with the adsorbent nanoparticles' binding sites. The endothermic nature of the suggested adsorption process is indicated by the rise in the %R and q_t values with temperature (Amar et al. 2021b; Badawy et al. 2023, 2021; Rehim et al. 2022). While ZnFe_2O_4 @silica is more active than ZnFe_2O_4 for the

adsorption of MB as the temperature rises, the nanoparticles prepared and activated at 600 °C have highly effective adsorption removal comparable to that activated at 800 °C. Meanwhile, ZnFe_2O_4 @silica has a removal efficiency of 91.58 at 50 °C compared to 86.22% for ZnFe_2O_4 . The findings suggested that higher temperatures within the proper temperature range were favoured for MB adsorption on the adsorbents. This result can be illustrated by the fact that the MB molecules' mobility and diffusion increased as the temperature rose, increasing their interaction with the active adsorption sites on the adsorbents (Mouni et al. 2018).

Adsorption thermodynamics

To explore the thermodynamics parameters for MB dye removal, the adsorption studies were calculated at temperatures ranging from 25 to 50 °C in 30 min of contact duration and 100 mg/L starting concentrations. Table 2 lists the thermodynamic parameters for the uptake of MB on ZnFe_2O_4 and ZnFe_2O_4 @silica surface activated at 600 and 800 °C. Equation 15 was used to compute the Gibb's free energy (ΔG°), and the intercept and slope of the Van't Hoff plot of $\ln K_d$ vs $1/T$ were used to design the values of the (ΔS°) and (ΔH°). Negative values of ΔG° (– 0.07 to – 0.826 kJ/mol) for ZnFe_2O_4 @Silica activated at 600 and 800 °C demonstrated thermodynamically spontaneous dye adsorption. The observed increase in negative values of ΔG° along with the rise in dye solution temperature suggests that MB adsorption was more effective at higher temperatures. Due to the non-spontaneous nature of the suggested adsorption process, ZnFe_2O_4 exhibits positive values of ΔG° at all temperatures. The MB adsorption is more advantageous on ZnFe_2O_4 @silica activated at 600 °C than ZnFe_2O_4 because the negative ΔG° values for adsorption are bigger on ZnFe_2O_4 @silica than ZnFe_2O_4 (Javed et al. 2018; Liu et al. 2010). The positive ΔH° values suggest that dye adsorption by samples constituted an endothermic reaction. ZnFe_2O_4 and ZnFe_2O_4 @silica nanoparticles both have positive ΔS° values, which

Fig. 8 a and b are the MB uptake percentage and adsorption capacity responses to solution temperature, respectively

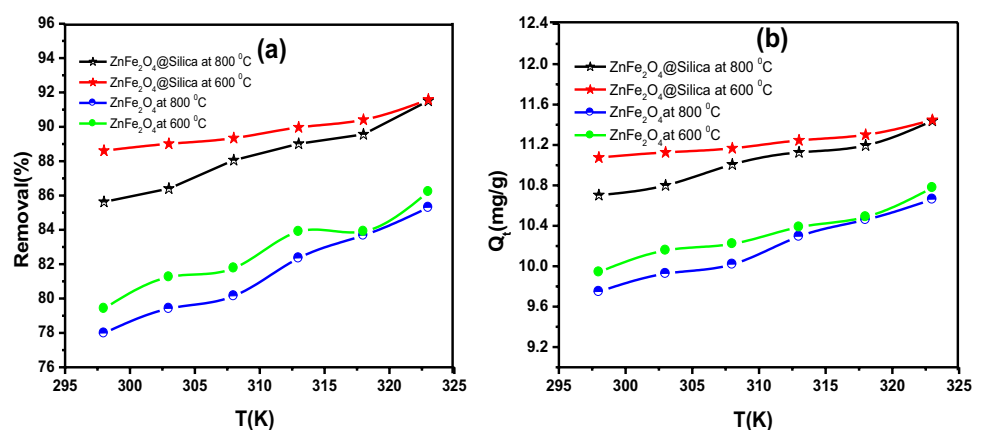


Table 3 Kinetic parameters for the adsorption of MB by ZnFe₂O₄ and ZnFe₂O₄@Silica nanoparticles

Adsorbent	Calc. temp., °C	$q_e^{exp.}$ (mg/g)	Pseudo-first order			Pseudo-second order		
			q_e^{cal}	k_1	R^2	q_e^{cal}	k_2	R^2
ZnFe ₂ O ₄	600	11.806	3.961	0.0183	0.7683	13.392	0.0038	0.9902
ZnFe ₂ O ₄	800	11.687	4.533	0.0211	0.7637	12.355	0.0072	0.9942
ZnFe ₂ O ₄ @silica	600	11.953	6.883	0.0395	0.8772	12.511	0.0127	0.9994
ZnFe ₂ O ₄ @silica	800	11.926	2.701	0.0232	0.9345	12.359	0.0139	0.9994

take into account the enhanced randomness at the interface of solid solution through the adsorption procedure (Liu 2009).

Adsorption kinetics

The MB uptake kinetics by ZnFe₂O₄ and ZnFe₂O₄@Silica nanoparticles were evaluated using linear pseudo-first-order (PFO) and pseudo-second-order (PSO) models. The fitting parameters for the models are listed in Table 3. For all manufactured nanoparticles, the correlation coefficient (R^2) value of the PSO model (0.9994) was higher than that of the PFO model, and in contrast to the PFO model, the estimated q_e value obtained from the PSO model was close to the experimental q_e value. This indicates that the PSO kinetic model, which quantifies the ratio of the occupancy rate of active sites by adsorbents, is squared by the number of unoccupied sites that better describes the proposed adsorption procedure (Nemati et al. 2021).

The adsorption mechanism was enhanced by the identification of the rate-controlling/determining step. The rate of adsorption may also be influenced by the intra-particle environment. The Weber-Morris intra-particle diffusion model was used to ascertain if intra-particle diffusion is the rate-limiting phase (Igwe et al. 2008, Mahto et al. 2014). The intra-particle diffusion could be shown as a linear plot of (q_t) vs ($t^{0.5}$) (c.f. Figure 9). The analysis of Fig. 9 revealed that there are three phases in the adsorption process. Following a curve, a second linear portion represents intra-particle diffusion, and the third stage is ascribed to equilibrium at the end, where the intra-particle diffusion slows down due to the extremely low bio-sorbate content that is still present in solution. Boundary layer diffusion is represented by the first linear segment. The value of the constant K_1 provided a notion of the boundary layer's thickness. Finding the step that determined rate, which was the slowest one, was crucial. The Boyd plot can be used to examine the kinetic data to determine this (c.f. Figure 10). The Boyd plot in Fig. 10 was linear and did not cross the origin, indicating that the external mass transfer mostly controls the reaction's rate. Table 4 demonstrates that ZnFe₂O₄@Silica had a higher computed intra-particle diffusion coefficient value R^2 than ZnFe₂O₄. These results indicate that ZnFe₂O₄@Silica exhibited higher diffusion than ZnFe₂O₄. These findings mean

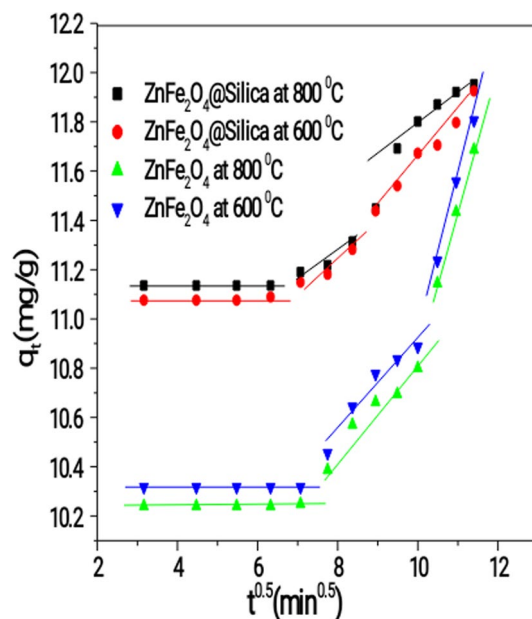


Fig. 9 Plot for evaluating rate constant of the intra-particle diffusion for sorption of MB on the synthesized ZnFe₂O₄ and ZnFe₂O₄@Silica nanoparticles

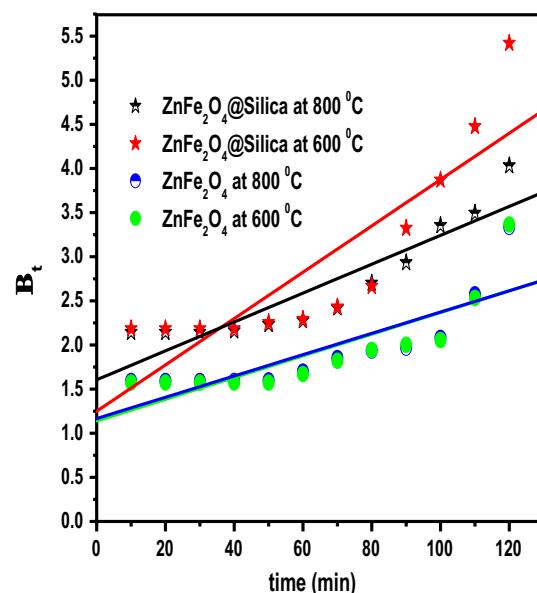


Fig. 10 Boyd plot for sorption of MB on the synthesized ZnFe₂O₄ and ZnFe₂O₄@Silica nanoparticles



Table 4 Intra-particle diffusion constants for ZnFe₂O₄ and ZnFe₂O₄@Silica nanoparticles

Adsorbent	Calc. temp., °C	K _{id}	C	R ²
ZnFe ₂ O ₄	600	0.0017	10.2323	0.4133
		0.1894	9.0325	0.9436
		0.6240	4.7015	0.9961
ZnFe ₂ O ₄	800	–	10.3176	P < 0.0001
		0.17	9.1081	0.9486
		0.5936	4.9297	0.9993
ZnFe ₂ O ₄ @Silica	600	–	11.1354	P < 0.0001
		0.0949	10.5077	0.8924
		0.1935	9.8048	0.8938
ZnFe ₂ O ₄ @Silica	800	0.00364	11.0614	0.5153
		0.1020	10.4157	0.9044
		0.1884	9.7554	0.9857

that diffusion by ZnFe₂O₄@Silica was higher than ZnFe₂O₄. Because the straight lines in these plots did not pass through the origin, it was clear that intra-particle diffusion was not the only rate-controlling step, suggesting that another diffusion model may have been used to identify the rate-controlling step (Ojediran et al. 2021). This means that the surface sorption contribution to the rate-determining of ZnFe₂O₄@Silica was more than that for ZnFe₂O₄, as seen by the rise in boundary thickness from the adsorbent ZnFe₂O₄ to ZnFe₂O₄@Silica. The thickness of the boundary layer was involved in the adsorption process when the thickness C of the adsorbents derived from the model was larger than zero.

Adsorption isotherms

The experimental adsorption data of MB by ZnFe₂O₄ and ZnFe₂O₄@Silica nanoparticles were fitted using Langmuir, Freundlich, Temkin, and DKR isotherm models, and the derived parameters of these isotherm models are provided in

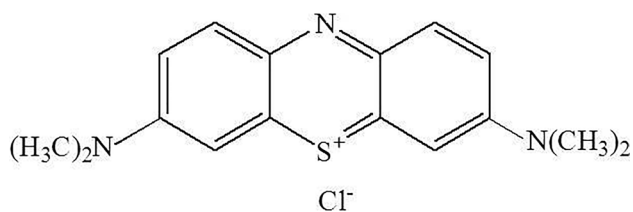
Table 5 Langmuir, Freundlich, Temkin, and DKR isotherm model constants and correlation coefficients for adsorption of MB by ZnFe₂O₄ and ZnFe₂O₄@Silica nanoparticles

Type of isotherm	Parameters	Adsorbent			
		ZnFe ₂ O ₄ at 600 °C	ZnFe ₂ O ₄ at 800 °C	ZnFe ₂ O ₄ @Silica at 600 °C	ZnFe ₂ O ₄ @Silica at 800 °C
Langmuir	q _m (mg/g)	0.0701	0.5309	0.5166	0.3994
	K _L (L/mg)	0.0938	0.0544	0.1116	0.1007
	R ²	0.8513	0.8201	0.5782	0.5455
Freundlich	n	0.0609	0.2455	0.1531	0.1429
	K _f	1.5955e-16	0.8681e-4	0.1003e-4	0.1745e-5
	R ²	0.9930	0.9207	0.9304	0.8971
Temkin	b _T (J/mol)	36.948	164.265	65.263	62.757
	K _T (L/g)	0.1158	0.1222	0.1683	0.1492
	R ²	0.6135	0.3818	0.7825	0.7693
DKR	Q _d	5.1284	13.6934	12.1971	17.2446
	A _{DKR}	1.345E-5	4.4978E-5	3.2538E-5	4.4063E-5
	E (kJ/mol)	0.5496	0.2267	0.2807	0.2297
	R ²	0.98024	0.84879	0.94554	0.92860

Table 5. Table 6 contains the derived separation factor (R_L)

Table 6 Dimensionless separation factor, R_L

Concentration of MB mg/l	Adsorbent			
	ZnFe ₂ O ₄ at 600 °C	ZnFe ₂ O ₄ at 800 °C	ZnFe ₂ O ₄ @Silica at 600 °C	ZnFe ₂ O ₄ @Silica at 600 °C
10	0.5158	0.6475	0.4727	0.4981
30	0.2531	0.3797	0.2301	0.2486
50	0.1756	0.2687	0.1520	0.1656
70	0.1321	0.2078	0.1135	0.1242
100	0.0963	0.1552	0.0823	0.0903
150	0.0663	0.10909	0.0564	0.0620
200	0.0506	0.0841	0.0429	0.0473

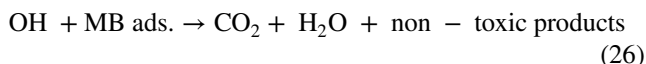
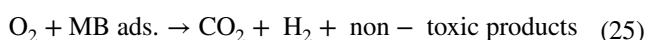
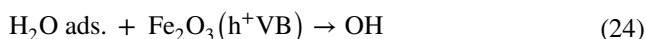
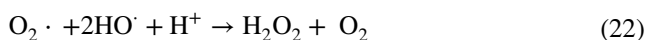
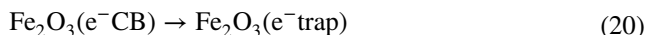
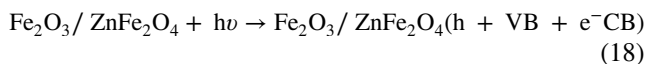


Scheme 1 Molecular structure of methylene blue dye

values. At various initial dye concentrations (10–200 mg/L), the values of R_L were less than unity. The information from Table 6 demonstrated that the Freundlich isotherm model had a greater correlation coefficient (R^2) value than the Langmuir isotherm model. As a result, it was inferred that the Freundlich isotherm model was a good fit for explaining the adsorption process. The slope and intercept were used using Temkin isotherm to get the equilibrium binding constant A_T (Lg^{-1}). A significant interaction between MB and the adsorbent surface was evident from the high A_T values. According to the values of A_T , $ZnFe_2O_4@Silica$ was more difficult to work with than $ZnFe_2O_4$ for MB. Based on R^2 value, $ZnFe_2O_4@Silica$ was nicely fitted into the DKR model. The Dubinin-Radushkevich model predicts the physical adsorption process by assuming that the adsorption is multi-layer in nature. Since physisorption was the adsorption process and the value of ΔE (the free energy of transfer of one solute from infinity to the surface of adsorbent) was less than 8 kJ/mol, Freundlich isotherm was further supported. The uptake of the MB dye by $ZnFe_2O_4$ and $ZnFe_2O_4@Silica$ was a multilayer, random process, according to the Freundlich isotherm (Scheme 1).

The most common factors determining adsorption performance are the resulting adsorbate's ability to bind dye molecules and the extent to which it influences the recombination of ($e^- + h^+$) pairs. Here, Fe_2O_3 can improve the adsorption activity of the samples by increasing their specific surface area, increasing the efficiency with which light is absorbed by their surface, and possibly speeding up the transfer of ($e^- + h^+$) pairs of Fe_2O_3 . Equations (18–26) explain the mechanism of the degradation of MB dye on the produced samples based on previous results. Using UV light to excite the electrons into the conduction band (CB) and the holes to remain in the valence band (VB), as outlined in Eq. (18), is the initial stage in creating the ($e^- + h^+$) pairs on the prepared samples. The recombination of the photogenerated pairs may be delayed as a result of the photogenerated e^- on the CB of $ZnFe_2O_4$ migrating to the CB of Fe_2O_3 instead of the VB (as shown in Eqs. (19–21)). Otherwise, superoxide radicals could be created when it combines with the dissolved oxygen. Equations (22 and 23) predict that when the generated superoxide radicals combine with water,

they will transform into hydroxide radicals. In addition, more hydroxyl radicals are generated Eq. (24), when the adsorbed water molecules react with the hydroxyl radicals at the $ZnFe_2O_4$ VB. The generated hydroxyl and superoxide radicals, which photodegrade the MB into CO_2 , water, and non-toxic chemicals, are powerful oxidizing species, according to Eqs. (25 and 26).



Comparison of different adsorbents' adsorption effectiveness with MB

Table 7 represents a comparison of removal % of MB by different adsorbents. According to the results, $ZnFe_2O_4$ and $ZnFe_2O_4@Silica$ nanoparticles are effective adsorbent materials for removing extremely hazardous cationic dye (MB) from wastewater.

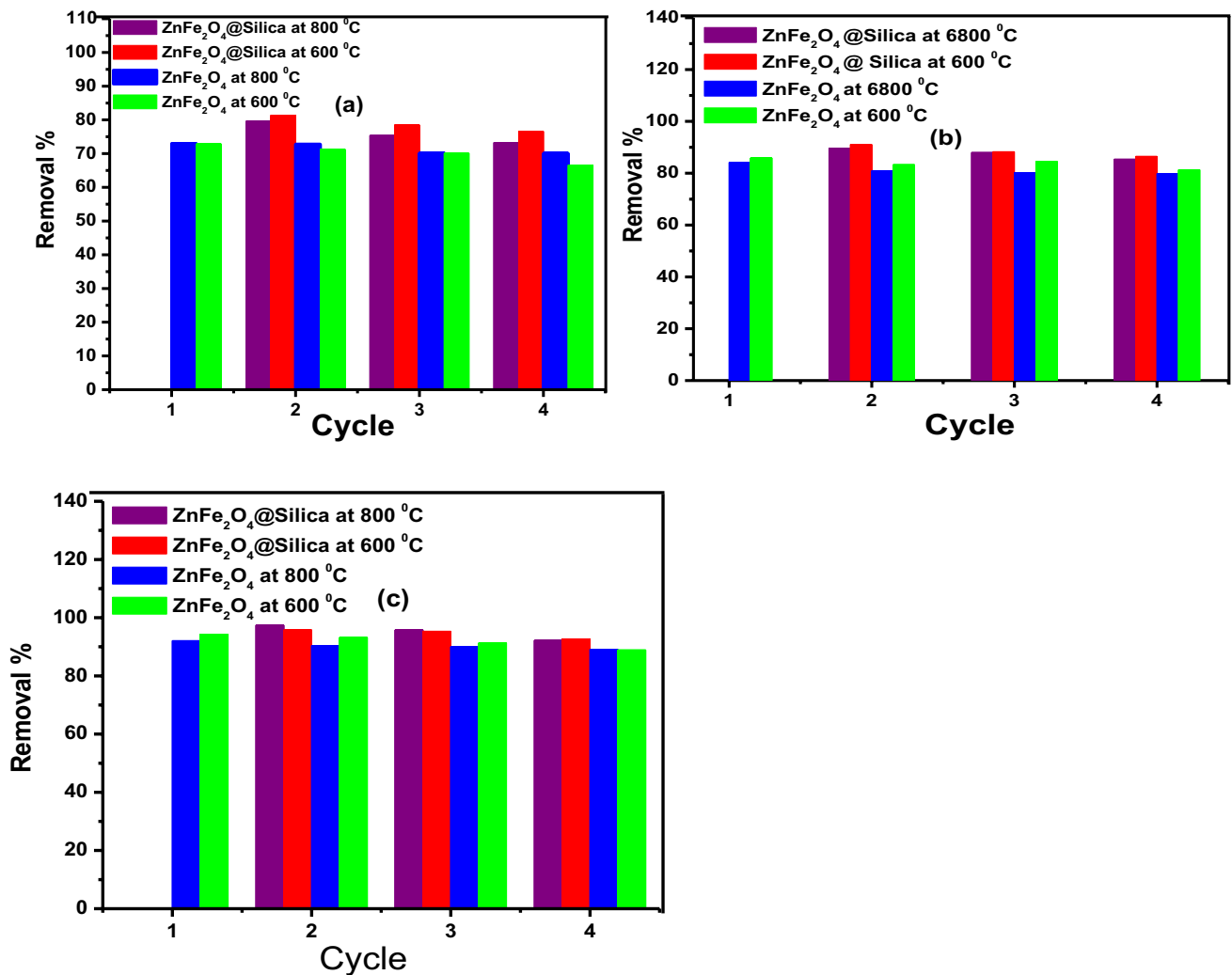
Desorption and regeneration study of the adsorbent

For the adsorbent to be commercially viable, desorption and regeneration research is crucial. 0.1 g of adsorbent and 25 mg/L of the MB dye concentration were typically stirred for 180 min. The analyte's ultimate concentration was calculated. The MB-loaded nanoparticle was eluted using 0.4, 0.5, and 0.6 M HNO_3 as the desorbing after the adsorption cycle. Desorbed nanoparticles were employed as the regenerated adsorbent for the subsequent adsorption cycle after the supernatant's MB dye content was determined. Desorption percentage of MB was found to be 72.9 and 73% for the first cycle for $ZnFe_2O_4$ at 600 and 800 °C, respectively, while the desorption percentage of MB by $ZnFe_2O_4@Silica$ at 600 and 800 °C was found 81.4 and 79.6% for the first



Table 7 Comparison of the uptake of MB onto different adsorbents

No	Adsorbent	(R%)	References
1	Reduced graphene oxide	29.26%	Siong et al. (Siong et al. 2019)
2	CoFe _{1.9} Mo _{0.1} O ₄	43%	Amar et al. (Amar et al. 2018)
3	Polyol-assisted NiFe ₂ O ₄	52%	Gayathri et al. (Gayathri et al. 2019)
4	Fe ₃ O ₄ /PCC MNPs	75.5%	Hua et al. (Hua et al. 2018)
5	Black Tea Wastes-Modified Nanocellulose	78%	Tsade Kara et al. (Tsade Kara et al. 2021)
6	ZnCl ₂ -Activated Corn Husk Carbon	95%	Khodaie et al. (Khodaie et al. 2013)
7	ZnF ₂ O ₄ at 600 °C	94.4%	This study
8	ZnF ₂ O ₄ at 800 °C	95.4%	
9	ZnF ₂ O ₄ @ Silica at 600 °C	95.46%	
10	ZnF ₂ O ₄ @ Silica at 800 °C	95.4%	

**Fig.11** The histogram of removal efficiency of MB by ZnFe₂O₄ and ZnFe₂O₄ @Silica with different concentrations of eluent **a:** 0.4 mol/L, **b:** 0.5 mol/L, and **c:** (0.6 mol/L)

two cycles by using 0.4 mol/L HNO₃. High concentration of HNO₃ resulted in the increase of the desorption percentage of MB for all nanoparticles prepared as shown in Fig. 11.

Hence, the synthesized nanoparticles can be used for more than 4 complete cycles of adsorption and desorption.



Conclusion

Nanozinc ferrite and that loaded at silica particles were successfully synthesized via precipitation process and activated at 600 and 800 °C. The XRD revealed that calcination temperature to 800 °C and presence of silica resulted in the appearance of ZnFe₂O₄ as the major phase and Fe₂O₃ as the minor phase. The adsorption properties of prepared adsorbents for the uptake of MB were inspected under various conditions. Nanoparticles activated at 600 °C more active than that at 800 °C. Also, nanozinc ferrite loaded at silica particles showed more efficiency for removal of MB than pure zinc ferrite and about 95% of MB was removed at pH 7. The data exhibited pseudo-second-order kinetic behaviour, according to the kinetic investigations. In order to understand the equilibrium between the adsorption of MB by ZnFe₂O₄ and ZnFe₂O₄@Silica, the Langmuir, Freundlich, Temkin, and Dubinin-Kaganer-Radushkevich (DKR) isotherm models were used. According to the thermodynamic analyses, it was possible, spontaneous, physical, and endothermic for MB to adsorb on ZnFe₂O₄ and ZnFe₂O₄@Silica. Since the straight lines in these plots did not pass through the origin, it was implied that intra-particle diffusion was not the only rate-controlling step and that another diffusion model could be employed to identify it. The findings indicated that ZnFe₂O₄ and ZnFe₂O₄@Silica are both suitable adsorbents for the adsorptive uptake of hazardous dyes from wastewater. ZnFe₂O₄@Silica nanoadsorbent has shown better MB removal than ZnFe₂O₄ adsorbent.

Funding Open access funding provided by The Science, Technology & Innovation Funding Authority (STDF) in cooperation with The Egyptian Knowledge Bank (EKB).

Data availability All data generated or analysed during this study are included in this published article.

Declarations

Conflict of Interest The authors declare that they have no conflict of interest.

Open Access This article is licensed under a Creative Commons Attribution 4.0 International License, which permits use, sharing, adaptation, distribution and reproduction in any medium or format, as long as you give appropriate credit to the original author(s) and the source, provide a link to the Creative Commons licence, and indicate if changes were made. The images or other third party material in this article are included in the article's Creative Commons licence, unless indicated otherwise in a credit line to the material. If material is not included in the article's Creative Commons licence and your intended use is not permitted by statutory regulation or exceeds the permitted use, you will need to obtain permission directly from the copyright holder. To view a copy of this licence, visit <http://creativecommons.org/licenses/by/4.0/>.

References

- Abubaker MA, Huo G, Shi J, Farah AA, Zhang J (2020) Removal of methylene blue from aqueous solutions using nano-magnetic adsorbent based on zinc-doped cobalt ferrite. *Chem Methodol* 4:1–18
- Al-Anber ZA, Al-Anber MA, Matouq M, Al-Ayed O, Omari NM (2011) Defatted Jajoba for the removal of methylene blue from aqueous solution: Thermodynamic and kinetic studies. *Desalination* 276(1–3):169–174
- Amar IA, Zayid EA, Dhikeel SA, Najem MY (2021a) Biosorption removal of methylene blue dye from aqueous solutions using phosphoric acid-treated balanites aegyptiaca seed husks powder. *Biointerface Res Appl Chem* 12:7845–7862
- Amar IA, Sharif A, Alkhalayali MM, Jabji MA, Altohami F, Qadir A, Ahwidi MM (2018) Adsorptive removal of methylene blue dye from aqueous solutions using CoFe_{1.9}Mo_{0.1}O₄ magnetic nanoparticles. *Iranian (Iranica). J Energy Environ* 4:247–254
- Amar IA, Asser JO, Mady AS, Abdulqadir MS, Altohami FA, Sharif AA, Abdalsamed IA (2021b) Adsorptive removal of congo red dye from aqueous solutions using Mo-doped CoFe₂O₄ magnetic nanoparticles. *Pigment Res Technol* 50(6):563–573
- Asfaram A, Ghaedi M, Hajati S, Rezaeinejad M, Goudarzi A, Purkait MK (2015) Rapid removal of Auramine-O and Methylene blue by ZnS: Cu nanoparticles loaded on activated carbon: a response surface methodology approach. *J Taiwan Inst Chem Eng* 53:80–91
- Badawy AA, Ghanem AF, Yassin MA, Youssef AM, Rehim MHA (2021) Utilization and characterization of cellulose nanocrystals decorated with silver and zinc oxide nanoparticles for removal of lead ion from wastewater. *Environ Nanotechnol Monit Manag* 16:100501
- Badawy AA, Rehim MHA, Turkey GM (2023) Charge transport and heavy metal removal efficacy of graphitic carbon nitride doped with CeO₂. *RSC Adv* 13(13):8955–8966
- Badawy AA, Ibrahim SM, Essawy HA (2020) Enhancing the textile dye removal from aqueous solution using cobalt ferrite nanoparticles prepared in presence of fulvic acid. *J Inorgan Organomet Polym Mater* 30:1798–1813
- Bangari RS, Yadav A, Sinha N (2021) Experimental and theoretical investigations of methyl orange adsorption using boron nitride nanosheets. *Soft Matter* 17(9):2640–2651
- Bayomie OS, Kandeel H, Shoeb T, Yang H, Youssef N, El-Sayed MM (2020) Novel approach for effective removal of methylene blue dye from water using fava bean peel waste. *Sci Rep* 10(1):7824
- Cheng J, Zhan C, Wu J, Cui Z, Si J, Wang Q, Peng X, Turng LS (2020) Highly efficient removal of methylene blue dye from an aqueous solution using cellulose acetate nanofibrous membranes modified by polydopamine. *ACS Omega* 5(10):5389–5400
- Dada AO, Adekola FA, Odeunmi EO (2017) A novel zerovalent manganese for removal of copper ions: synthesis, characterization and adsorption studies. *Appl Water Sci* 7:1409–1427
- Dindorkar SS, Patel RV, Yadav A (2022) Adsorptive removal of methylene blue dye from aqueous streams using photocatalytic CuBTC/ZnO chitosan composites. *Water Sci Technol* 85(9):2748–2760
- Dinh VP, Le HM, Nguyen VD, Dao VA, Hung NQ, Tuyen LA, Lee S, Yi J, Nguyen TD, Tan LV (2019) Insight into the adsorption mechanisms of methylene blue and chromium (III) from aqueous solution onto pomelo fruit peel. *RSC Adv* 9(44):25847–25860
- Dubinin MM (1965) Modern state of the theory of volume filling of micropore adsorbents during adsorption of gases and steams on carbon adsorbents. *Zh Fiz Khim* 39(19):1305–1317
- ElHarby N, Badawy A, Ibrahim S (2019) Improvement of Nanosized CuO-Fe₂O₃/cordierite System by Li₂O-treatment for wastewater treatment. *J Ultrafine Grained Nanostruct Mater* 52(2):175–187



- Freundlich HMF (1906) Over the adsorption in solution. *J Phys Chem* 57(385471):1100–1107
- Gayathri MB, Mathangi JB, Raji P, Helen K (2019) M, Equilibrium and kinetic studies on methylene blue adsorption by simple polyol assisted wet hydroxyl route of NiFe₂O₄ nanoparticles. *J Environ Health Sci Eng* 17(2):539–547
- Ghanem AF, Badawy AA, Mohram ME, Rehim MHA (2020) Synergistic effect of zinc oxide nanorods on the photocatalytic performance and the biological activity of graphene nano sheets. *Heliyon* 6(2):e03283
- Hajjalilgol S, Masoum S (2019) Optimization of biosorption potential of nano biomass derived from walnut shell for the removal of malachite green from liquids solution: experimental design approaches. *J Mol Liq* 286:110904
- Heidarinejad Z, Rahmani O, Fazlzadeh M, Heidari M (2018) Enhancement of methylene blue adsorption onto activated carbon prepared from Date Press Cake by low frequency ultrasound. *J Mol Liq* 264:591–599
- Hua Y, Xiao J, Zhang Q, Cui C, Wang C (2018) Facile synthesis of surface-functionalized magnetic nanocomposites for effectively selective adsorption of cationic dyes. *Nanoscale Res Lett* 13:1–9
- Huang Y, Farooq MU, Lai S, Feng X, Sampranpiboon P, Wang X, Huang W (2018) Model fitting of sorption kinetics data: Misapplications overlooked and their rectifications. *AIChE J* 64(5):1793–1805
- Ibrahim SM, Badawy AA, Essawy HA (2019) Improvement of dyes removal from aqueous solution by Nanosized cobalt ferrite treated with humic acid during coprecipitation. *J Nanostruct Chem* 9:281–298
- Ibrahim SM, Ghanem AF, Sheir DH, Badawy AA (2022) Effective single and contest carcinogenic dyes adsorption onto A-zeolite/bacterial cellulose composite membrane: Adsorption isotherms, kinetics, and thermodynamics. *J Environ Chem Engin* 10(6):108588
- Igwe JC, Abia AA, Ibeh CA (2008) Adsorption kinetics and intraparticle diffusivities of Hg, As and Pb ions on unmodified and thiolated coconut fiber. *Int J Environ Sci Technol* 5:83–92
- Javed H, Luong DX, Lee CG, Zhang D, Tour JM, Alvarez PJ (2018) Efficient removal of bisphenol-A by ultra-high surface area porous activated carbon derived from asphalt. *Carbon* 140:441–448
- Kefeni KK, Mamba BB, Msagati TA (2017) Application of spinel ferrite nanoparticles in water and wastewater treatment: a review. *Sep Purif Technol* 188:399–422
- Khodaie M, Ghasemi N, Moradi B and Rahimi M, (2013) Removal of methylene blue from wastewater by adsorption onto ZnCl₂ activated corn husk carbon equilibrium studies. *J Chem*
- Kumar M, Dossanj HS, Singh H (2017) Synthesis of spinel ZnFe₂O₄ modified with SDS via low temperature combustion method and adsorption behaviour of crystal violet dye. *Asian J Chem* 29(9):2057–2064
- Langmuir I (1916) The constitution and fundamental properties of solids and liquids. Part I. Solids. *J Am Chem Soc* 38(11):2221–2295
- Lei D, Xue J, Peng X, Li S, Bi Q, Tang C, Zhang L (2021) Oxalate enhanced synergistic removal of chromium (VI) and arsenic (III) over ZnFe₂O₄/g-C₃N₄: Z-scheme charge transfer pathway and photo-Fenton like reaction. *Appl Catal B* 282:119578
- Lim LB, Priyantha N, Tennakoon DTB, Chieng HI, Dahri MK, Suklueng M (2017) Breadnut peel as a highly effective low-cost biosorbent for methylene blue: equilibrium, thermodynamic and kinetic studies. *Arab J Chem* 10:S3216–S3228
- Liu Y (2009) Is the free energy change of adsorption correctly calculated. *J Chem Eng Data* 54(7):1981–1985
- Liu QS, Zheng T, Wang P, Jiang JP, Li N (2010) Adsorption isotherm, kinetic and mechanism studies of some substituted phenols on activated carbon fibers. *Chem Eng J* 157(2–3):348–356
- Liu F, Zhou K, Chen Q, Wang A, Chen W (2018) Comparative study on the synthesis of magnetic ferrite adsorbent for the removal of Cd (II) from wastewater. *Adsorpt Sci Technol* 36(7–8):1456–1469
- Maddalena R, Hall C, Hamilton A (2019) Effect of silica particle size on the formation of calcium silicate hydrate [CSH] using thermal analysis. *Thermochim Acta* 672:142–149
- Mahmoodi NM, Abdi J, Bastani D (2014) Direct dyes removal using modified magnetic ferrite nanoparticle. *J Environ Health Sci Eng* 12:1–10
- Mahto TK, Chowdhuri AR, Sahu SK (2014) Polyaniline-functionalized magnetic nanoparticles for the removal of toxic dye from wastewater. *J Appl Polym Sci*, 131(19)
- Mapossa AB, Mhike W, Adalima JL, Tichapondwa S (2021) Removal of organic dyes from water and wastewater using magnetic ferrite-based titanium oxide and zinc oxide nanocomposites: a review. *Catalysts* 11(12):1543
- Mapossa AB, Dantas J, Silva MR, Kiminami RH, Costa ACF, Daramola MO (2020) Catalytic performance of NiFe₂O₄ and Ni_{10.3}Zn_{0.7}Fe₂O₄ magnetic nanoparticles during biodiesel production. *Arab J Chem* 13(2):4462–4476
- Mouni L, Belkhir L, Bollinger JC, Bouzaza A, Assadi A, Tirri A, Dahmoune F, Madani K, Remini H (2018) Removal of Methylene Blue from aqueous solutions by adsorption on Kaolin: Kinetic and equilibrium studies. *Appl Clay Sci* 153:38–45
- Nady N, Abdel Rehim MH, Badawy AA (2023) Dye removal membrane from electrospun nanofibers of blended polybutylenesuccinate and sulphonated expanded polystyrene waste. *Sci Rep* 13(1):15455
- Nemati F, Jafari D, Esmaeili H (2021) Highly efficient removal of toxic ions by the activated carbon derived from Citrus limon tree leaves. *Carbon Lett* 31(3):509–521
- Ojediran JO, Dada AO, Aniyi SO, David RO, Adewumi AD (2021) Mechanism and isotherm modeling of effective adsorption of malachite green as endocrine disruptive dye using Acid Functionalized Maize Cob (AFMC). *Sci Rep* 11(1):21498
- Rehim MHA, Badawy AA, Turkey G (2022) Electrical properties and heavy ions removal ability of graphitic carbon nitride/polypyrrole composite. *J Phys Chem Solids* 167:110741
- Shindhal T, Rakholiya P, Varjani S, Pandey A, Ngo HH, Guo W, Ng HY, Taherzadeh MJ (2021) A critical review on advances in the practices and perspectives for the treatment of dye industry wastewater. *Bioengineered* 12(1):70–87
- Siong VLE, Lee KM, Juan JC, Lai CW, Tai XH, Khe CS (2019) Removal of methylene blue dye by solvothermally reduced graphene oxide: a metal-free adsorption and photodegradation method. *RSC Adv* 9(64):37686–37695
- Temkin MJ, and Pyzhev V (1940) Recent modifications to Langmuir isotherms. 217–222
- Tran HN, You SJ, Hosseini-Bandegharaei A, Chao HP (2017) Mistakes and inconsistencies regarding adsorption of contaminants from aqueous solutions: a critical review. *Water Res* 120:88–116
- Tsade Kara H, Anshebo ST, Sabir FK, Adam Workineh G (2021) Removal of methylene blue dye from wastewater using periodiated modified nanocellulose. *Int J Chem Eng* 2021:1–16
- Ullah A, Zahoor M, Din WU, Muhammad M, Khan FA, Sohail A, Ullah R, Ali EA, Murthy HA (2022) Removal of methylene blue from aqueous solution using black tea wastes: used as efficient adsorbent. *Adsorpt Sci Technol* 2022:1–9
- Vadivelan V, Kumar KV (2005) Equilibrium, kinetics, mechanism, and process design for the sorption of methylene blue onto rice husk. *J Colloid Interface Sci* 286(1):90–100
- Weber TW, Chakravorti RK (1974) Pore and solid diffusion models for fixed-bed adsorbers. *AIChE J* 20(2):228–238
- Yadav A, Bagotia N, Sharma AK, Kumar S (2021) Advances in decontamination of wastewater using biomass-based composites: A critical review. *Sci Total Environ* 784:147108
- Yadav A, Patel RV, Singh CP, Labhasetwar PK, Shahi VK (2022) Experimental study and numerical optimization for removal of methyl orange using polytetrafluoroethylene membranes in vacuum membrane distillation process. *Colloids Surf A* 635:128070



- Yaseen DA, Scholz M (2019) Textile dye wastewater characteristics and constituents of synthetic effluents: a critical review. *Internat J Environ Sci Technol* 16:1193–1226
- Zhao X, Baharinikoo L, Farahani MD, Mahdizadeh B, Farizhandi AAK (2022) Experimental modelling studies on the removal of dyes and heavy metal ions using ZnFe_2O_4 nanoparticles. *Sci Rep* 12(1):5987